

Sparse Bayesian Deep Learning for Dynamic System Identification

Hongpeng Zhou, Chahine Ibrahim, Wei Xing Zheng, and Wei Pan

Abstract—This paper proposes a sparse Bayesian treatment of deep neural networks (DNNs) for system identification. Although DNNs show impressive approximation ability in various fields, several challenges still exist for system identification problems. First, DNNs are known to be too complex that they can easily overfit the training data. Second, the selection of the input regressors for system identification is nontrivial. Third, uncertainty quantification of the model parameters and predictions are necessary. The proposed Bayesian approach offers a principled way to alleviate the above challenges by marginal likelihood/model evidence approximation and structured group sparsity-inducing priors construction. The identification algorithm is derived as an iterative regularized optimization procedure that can be solved as efficiently as training typical DNNs. Furthermore, a practical calculation approach based on the Monte-Carlo integration method is derived to quantify the uncertainty of the parameters and predictions. The effectiveness of the proposed Bayesian approach is demonstrated on several linear and nonlinear systems identification benchmarks with achieving good and competitive simulation accuracy.

Index Terms—Regularized System Identification, Deep Neural Networks, Group Sparsity, Sparse Bayesian Learning.

I. INTRODUCTION

System identification (SYSID) has a long history in natural and social sciences [17]. Various approaches have been proposed for both linear/nonlinear systems and static/dynamical processes [36], [2], [8], [21]. Among these, neural networks (NNs) are prominent black-box models and recently regain research interest in the SYSID community [19], [6], thanks to the boom of deep learning.

The deep neural network (DNN) models have their advantages and disadvantages. An early paper on feed-forward NNs proved the universal approximation capabilities of any measurable function, using one hidden layer on a compact set [16]. Several works also achieved competitive results by using feed-forward NNs [22] and recurrent neural networks (RNNs) [3] in the context of dynamical systems. However, it is not easy to design a proper NN structure. First of all, the trade-off between the model complexity and (simulation) prediction accuracy should be considered. An over-simplified model cannot reveal the underlying relation between input data and output data. On the other hand, an over-complex model may overfit

The authors Hongpeng Zhou, Chahine Ibrahim and Wei Pan are with the Faculty of Mechanical, Maritime and Materials Engineering, Delft University of Technology, 2628 CD, Delft, the Netherlands (email: h.zhou-3@tudelft.nl, ibrahim-chahine@outlook.com, wei.pan@tudelft.nl. Corresponding author Wei Pan.).

Wei Xing Zheng is with the School of Computer, Data and Mathematical Sciences, Western Sydney University, Sydney, NSW 2751, Australia (email: W.Zheng@westernsydney.edu.au)

the training data, thus reducing its generalization ability. Besides, inevitable (non-Gaussian and non-additive) noise and non-smooth characteristics of some nonlinear processes may also cause the overfitting problem. Furthermore, NNs can also be underspecified by the data and constitute a large space of hypotheses for high-performing models [4]. Another challenging problem for SYSID is input regressor selection, which is defined as follows: given input regressors $z(t+1) = [u(t+1), u(t), \dots, u(t-l_u), y(t), y(t-1), \dots, y(t-l_y)]^\top \in \mathbb{R}^{l_u+l_y+1}$ with l_u and l_y denoting respectively the input and output lag, the most relevant input regressor features, which can explain the intrinsic phenomenon of the system, are selected [7]. An effective input regressor selection can improve the prediction performance, and generalization ability of the identified model.

For these challenges, the sparse Bayesian learning method offers a principled way to tackle them simultaneously: a) A more efficient exploration of the hypothesis space (corresponding to saddle points) of NN models is possible [4], [9]; b) Over-fitting can be alleviated, and model redundancies can be eliminated through marginalization and by choice of sparsity inducing prior distribution over parameters [20]; c) Important input variables can be selected automatically by imposing structured sparsity on the NN; d) Model parameters and prediction uncertainties can be quantified, which is particularly useful in decision making and safety-critical applications such as autonomous driving and structural health monitoring [45].

Diverse Bayesian SYSID methods have been developed in the last decades. To name a few, a practical sparse Bayesian approach to state-space identification of nonlinear systems was proposed in [40] in the context of biochemical networks. A Bayesian identification algorithm of nonlinear autoregressive exogenous (NARX) models using variational inference with a demonstration on the electroactive polymer was introduced in [42]. A framework for identifying the governing interactions and transition logics of subsystems in cyber-physical systems was presented in [46] by using Bayesian inference and pre-defined basis functions. A variational expectation maximization approach to SYSID when the data includes outliers was developed in [23]. Two approaches to SYSID using Bayesian networks were proposed in [2]. The first one combines kernel-based stable spline and group Least Angle Regression while the other combines stable splines with the hyper-prior definition in a fully Bayesian model. However, this work did not discuss how to apply the Bayesian approach to the NN model. Another typical probabilistic nonparametric modeling method is the Gaussian process (GP), which can perform excellently for linear and

nonlinear SYSID tasks, but suffers from the high computational burden for large datasets and cannot conduct input regressor selection efficiently. Overall, specific to the use of NNs as a model form, little attention has been given to the identification of dynamic systems in a Bayesian framework.

Several approaches have been proposed to treat the NNs in a Bayesian manner, e.g., Laplace approximation, expectation propagation, variational inference, etc. Among these methods, the Laplace approximation is an approximated inference approach that can only represent local properties but is closer in efficiency to maximum a posteriori (MAP) [20]. However, to update the posterior variance of parameters, the Laplace approximation method requires computing the inverse Hessian of log-likelihood, which is infeasible for large-scale NNs. To address this issue, a fast Hessian calculation technique was devised for convolutional NNs and successfully obtains a impressive image classification performance [9]. Furtermore, we will also develop a companion technique for RNNs in this work.

In this paper, a sparse Bayesian approach is proposed to address several challenges for system identification based on deep neural networks, including overfitting the training data, the selection of the input regressors, and the uncertainty quantification of model parameters. We will consider two typical DNNs, i.e., Multi-Layer Perceptron (MLP) and Long Short-Term Memory networks (LSTM). The simulation error is adopted as the evaluation metric, which is a more challenging criterion compared with one-step-ahead prediction. The simulation error is equivalent to the N -step-ahead prediction error with N denoting a user-defined temporal horizon. In order to identify the system in a Bayesian framework, the group priors are introduced over network parameters to induce structured sparsity, and the Laplace approximation is used to approximate the intractable integral of the evidence. The main contributions of this paper have three folds:

- A practical iterative algorithm using Bayesian deep learning is proposed for SYSID. The first identification cycle of the algorithm is equivalent to the conventional sparse group lasso regularization method. This algorithm can be used with both MLP and LSTM networks for linear and nonlinear processes.
- The structured sparsity is incorporated in the Bayesian formulation of the identification problem to alleviate the overfitting issue and perform the selection of the input regressor. As a consequence, the number of hidden neurons in both MLP and LSTM networks can be significantly reduced.
- The proposed algorithm achieves good and competitive simulation accuracy on five benchmark datasets. The datasets of three linear processes are provided in the MATLAB System Identification Toolbox*, including the Hairdryer, Heat exchanger, and the Glass Tube manufacturing process. The datasets of two nonlinear processes are provided in the Nonlinear System Identification Benchmarks website†, includ-

ing the Cascaded Tanks [26] and Coupled Electric Drives [38].

The organization of this paper is as follows. Section II formulates the identification problem using DNNs and introduces the Bayesian approach. Section III presents the iterative procedure of the proposed sparse Bayesian learning algorithm and a recursive Hessian computation method. The illustration of structured sparsity regularization, uncertainty quantification, and the proposed training algorithm are introduced in Section IV. The identification results and detailed analysis are given in Section V. Section VI concludes the paper. A discussion on the limitations and future work are also included in Section VII.

II. PRELIMINARIES

A. Problem formulation

The chosen mathematical model structure is generated by training the network $\text{Net}(\mathcal{W}, z)$, where \mathcal{W} represents an array of the weights in the network and z represents the input regressors of size $1 \times (l_y + l_u + 1)$. These are best defined by the prediction model:

$$\hat{y}(t+1) = \text{Net}(\mathcal{W}, z(t+1), \epsilon) \quad (1)$$

where ϵ represents the noise term. It should be noted that the ϵ can be in any distribution of exponential family. And the model parameter can be identified with a maximum likelihood method in the case of Gaussian noise (see Chapter 7.3 in [17]). The input regressor of the model is defined as a combination of lagged elements of the system input u and outputs y . The input lag is denoted l_u and output lag l_y , resulting in the expression $z(t+1) = [u(t+1), u(t), \dots, u(t-l_u), y(t), y(t-1), \dots, y(t-l_y)]^\top$.

The first DNN model considered is the LSTM network, a type of RNN. Benefiting from the advantages of processing sequential data and memorizing information, LSTM can also be applied straightforwardly for dynamic SYSID [3]. The backpropagation through time (BPTT) method is used to train LSTM, where the network is unfolded in time and weights are updated based on an accumulation of gradients across time steps.

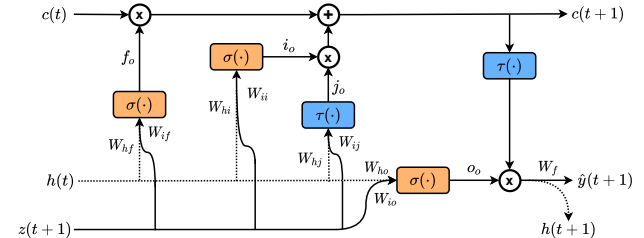


Fig. 1: Single layer long short term memory network.

The second DNN model considered is the MLP, a type of feed-forward NN. Backpropagation with stochastic gradient descent algorithm and variations are often used to train a MLP network.

B. Learning in a Bayesian framework

Given a dataset \mathcal{D} , the posterior estimation for network weights \mathcal{W} is given by Bayes' rule:

$$p(\mathcal{W}|\mathcal{D}, \mathcal{H}) = \frac{p(\mathcal{D}|\mathcal{W}, \mathcal{H})p(\mathcal{W}, \mathcal{H})}{p(\mathcal{D}|\mathcal{H})} \quad (2)$$

*<https://nl.mathworks.com/help/ident/examples.html>

†<https://sites.google.com/view/nonlinear-benchmark/>

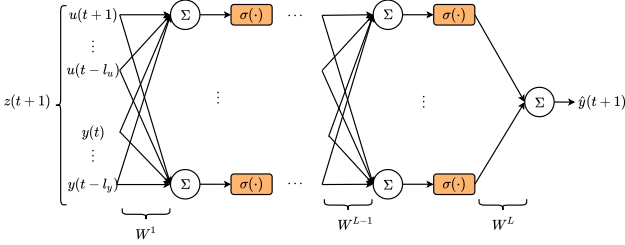


Fig. 2: Multi-Layer Perceptron with L layers

$p(\mathcal{D}|\mathcal{W}, \mathcal{H})$ designates the likelihood function, where $p(\mathcal{W}, \mathcal{H})$ denotes the prior over the weights \mathcal{W} and $p(\mathcal{D}|\mathcal{H})$ is the evidence of the hypothesis \mathcal{H} given \mathcal{D} . The hypothesis generally incorporates model and inference assumptions. For simplicity of notations, the hypothesis term is dropped in the rest of the paper. Assume that the likelihood function belongs to the exponential family:

$$\begin{aligned} p(\mathcal{D}|\mathcal{W}, \theta) &= g(\theta) \exp \left\{ \sum_{t=1}^T \eta_t(\mathcal{W}, \sigma) T_t(\sigma) + B(\mathcal{W}) \right\} \\ &= g(\theta) \exp \left\{ -\mathbf{E}(\mathcal{W}, \theta) \right\} \end{aligned} \quad (3)$$

where $g(\cdot), T_t(\cdot), \eta_t(\cdot)$ and $B(\cdot)$ are known functions corresponding to a specific exponential family distribution, θ is the parameter of the family, and $\mathbf{E}(\mathcal{W}, \theta)$ denotes an energy function.

The prior probabilities $p(\mathcal{W})$ takes a Gaussian relaxed variational form $p(\mathcal{W}) \geq p(\mathcal{W}, \psi) = \mathcal{N}(\mathcal{W}|0, \Psi) \phi(\psi)$, where $\phi(\psi)$ represents the hyperprior probability of $\psi \triangleq [\psi_{11}^1, \dots, \psi_{n_1 1}^1, \dots, \psi_{n_1 n_2}^1, \dots, \psi_{11}^L, \dots, \psi_{n_{L-1} n_L}^L]$ and $\Psi \triangleq \text{diag}(\psi)$. With the principle of minimizing the misaligned probability mass, the hyper-parameter ψ can be obtained by

$$\begin{aligned} \hat{\psi} &= \underset{\psi \geq 0}{\text{argmin}} \int p(\mathcal{D}|\mathcal{W}, \theta) |p(\mathcal{W}) - p(\mathcal{W}, \psi)| d\mathcal{W} \\ &= \underset{\psi \geq 0}{\text{argmax}} \int p(\mathcal{D}|\mathcal{W}, \theta) p(\mathcal{W}, \psi) d\mathcal{W}. \end{aligned} \quad (4)$$

The resulting problem is known as a type II maximum likelihood. The integration is intractable and can be obtained by the Laplace approximation method, which is explained in detail in Section. III-A.

III. SPARSE BAYESIAN DEEP LEARNING

A. Laplace approximation

The Laplace approximation method is adopted to compute the intractable integral in Eq. (4). $\mathbf{L}(\mathcal{W}, \theta)$ can be approximated by a second-order Taylor series expansion around a set of connection weights \mathcal{W}^* with the operator $\Delta\mathcal{W} = \mathcal{W} - \mathcal{W}^*$, so we have

$$\mathbf{E} \approx \mathbf{L}(\mathcal{W}^*, \theta) + \frac{1}{2} \Delta\mathcal{W}^T \mathbf{H} \Delta\mathcal{W} + \Delta\mathcal{W}^T \mathbf{g}. \quad (5)$$

The resulting expression for the likelihood in a compact form is given by

$$\begin{aligned} p(\mathcal{D}|\mathcal{W}, \theta) &= \mathbf{A}(\mathcal{W}^*, \theta) \exp \left\{ -\frac{1}{2} \mathcal{W}^T \mathbf{H} \mathcal{W} - \mathcal{W}^T \mathbf{g} \right\} \\ \hat{\mathbf{g}}(\mathcal{W}^*, \theta) &= \mathbf{g}(\mathcal{W}^*, \theta) - \mathbf{H}(\mathcal{W}^*, \theta) \mathcal{W}^* \end{aligned} \quad (6)$$

where $\mathbf{H}(\mathcal{W}^*, \theta)$ and $\mathbf{g}(\mathcal{W}^*, \theta)$ are respectively the Hessian and the gradient of the loss function \mathbf{E} with respect to \mathcal{W} at \mathcal{W}^* . Eq. (6) is obtained by grouping elements independent of the target variable \mathcal{W} in $\mathbf{A}(\mathcal{W}^*, \theta)$. The approximated likelihood is an exponent of a quadratic function corresponding to the Taylor series expansion of the energy loss. This form can be recast into a Gaussian function. In effect of the conjugacy of the prior and posterior, the posterior is Gaussian with mean and variance being

$$\mu_{\mathcal{W}} = \Sigma_{\mathcal{W}} \hat{\mathbf{g}} \quad \Sigma_{\mathcal{W}} = [\mathbf{H} + \Psi^{-1}]^{-1}. \quad (7)$$

A more detailed derivation of the Laplace approximation is given in Appendix A.

B. Evidence maximization

The evidence in Eq. (4) attempts to find the volume of the product $p(\mathcal{D}|\mathcal{W}, \theta)p(\mathcal{W}, \psi)$, which is Gaussian and proportional to the posterior. Thus, one can approximate the evidence as the volume around the most probable value (here the posterior $\mu_{\mathcal{W}}$).

$$\hat{\psi} = \underset{\psi \geq 0}{\text{argmax}} \int p(\mathcal{D}|\mathcal{W}, \theta) p(\mathcal{W}|\psi) p(\psi) d\mathcal{W} \quad (8)$$

$$\approx \underset{\psi \geq 0}{\text{argmax}} \underbrace{p(\mathcal{D}|\mu_{\mathcal{W}}, \theta)}_{\text{Best Fit Likelihood}} \underbrace{p(\mu_{\mathcal{W}}|\psi) |\Sigma_{\mathcal{W}}|^{\frac{1}{2}}}_{\text{Occam Factor}}. \quad (9)$$

In David Mackay's words, the evidence is approximated by the product of the data likelihood given the most probable weights and the Occam factor [20]. It can also be interpreted as a Riemann approximation of the evidence, where the best-fit likelihood represents the peak of the evidence. And the Occam's factor is the Gaussian curvature around the peak.

By realizing that the posterior mean $\mu_{\mathcal{W}}$ maximizes $p(\mathcal{D}|\mathcal{W}, \theta)p(\mathcal{W}|\psi)$, Eq. (9) can be rewritten into a joint maximization in \mathcal{W} and ψ . By applying the $-2 \log(\cdot)$ operation, the evidence maximization in Eq. (4) can be recast into a joint minimization of an objective function $\mathcal{L}(\mathcal{W}, \psi, \theta)$ given by:

$$\begin{aligned} \mathcal{L}(\mathcal{W}, \psi, \theta) &= \mathcal{W}^T \mathbf{H} \mathcal{W} + 2\mathcal{W}^T \hat{\mathbf{g}} + \mathcal{W}^T \Psi^{-1} \mathcal{W} + \log |\Psi| \\ &\quad + \log |\mathbf{H} + \Psi^{-1}| - T \log(2\pi\theta) \end{aligned} \quad (10)$$

For a more thorough mathematical derivation that leads to Eq. (10) and insight into the Laplace approximation, please refer to Appendix A and B.

C. Convex-concave procedure

The objective function in Eq. (10) can be seen as a sum of a convex u and concave v functions in ψ with:

$$u(\mathcal{W}, \psi) = \mathcal{W}^T \mathbf{H} \mathcal{W} + 2\mathcal{W}^T \hat{\mathbf{g}} + \mathcal{W}^T \Psi^{-1} \mathcal{W} \quad (11)$$

$$v(\psi) = \log |\Psi| + \log |\mathbf{H} + \Psi^{-1}|. \quad (12)$$

$\mathcal{W}^T \Psi^{-1} \mathcal{W}$ is positive definite, since $\psi > 0$. Thus, u is convex in Ψ . v can be reformulated as a log-determinant of an affine function of Ψ . By using the Schur complement determinant identity:

$$|\Psi| |\mathbf{H} + \Psi^{-1}| = \begin{vmatrix} \mathbf{H} & \\ & -\Psi \end{vmatrix} = |\mathbf{H}| |\mathbf{H}^{-1} + \Psi| \quad (13)$$

and taking the log of Eq.(13),

$$\log |\Psi| + \log |\mathbf{H} + \Psi^{-1}| = \log |\mathbf{H}| + \log |\mathbf{H}^{-1} + \Psi|$$

one finds an equivalent expression of v that is concave in Ψ . The minimization problem can therefore be reformulated as a convex-concave procedure (CCCP) [36]. \mathcal{W} and ψ are obtained by the iterative minimization of Eq. (14)-(15).

$$\mathcal{W}(k+1) = \underset{\mathcal{W}}{\operatorname{argmin}} u(\mathcal{W}, \psi(k)) \quad (14)$$

$$\psi(k+1) = \underset{\psi \geq 0}{\operatorname{argmin}} u(\mathcal{W}(k+1), \psi) + \alpha(k) \cdot \psi \quad (15)$$

where $\alpha(k) = \nabla_{\psi} v(\psi(k))^T$ is the gradient of v evaluated at the current iterate $\psi(k)$. Using the chain rule, its analytical form is given by:

$$\begin{aligned} \alpha(k) &= \nabla_{\psi} \left(\log |\Psi| + \log |\mathbf{H} + \Psi^{-1}| \right) \Big|_{\psi=\psi(k)} \\ &= -\operatorname{diag}(\Psi^{-1}(k)) \odot \operatorname{diag}((\mathbf{H} + \Psi^{-1}(k))^{-1}) \\ &\quad \odot \operatorname{diag}(\Psi^{-1}(k)) + \operatorname{diag}(\Psi^{-1}(k)) \end{aligned} \quad (16)$$

\odot is the point-wise Hadamard product. Since Ψ is a diagonal matrix, Eq. (15) can be expressed per connection independently. With $\Sigma_{W_{ab}^l}(k)$ being the connection weight posterior variance, the analytical form for α is:

$$\Sigma_{\mathcal{W}}(k) = (\mathbf{H}(k) + \Psi(k)^{-1})^{-1} \quad (17)$$

$$\alpha_{ab}^l(k) = -\frac{\Sigma_{W_{ab}^l}(k)}{\psi_{ab}^l(k)^2} + \frac{1}{\psi_{ab}^l(k)}. \quad (18)$$

The optimization step in Eq. (15) for ψ_{ab}^l becomes

$$\psi_{ab}^l(k+1) = \underset{\psi \geq 0}{\operatorname{argmin}} \frac{W_{ab}^l(k+1)^2}{\psi} + \alpha_{ab}^l(k) \cdot \psi. \quad (19)$$

By noting that

$$\frac{W_{ab}^l}{\psi} + \alpha_{ab}^l \cdot \psi \geq 2 \left| \sqrt{\alpha_{ab}^l} \cdot W_{ab}^l \right| \quad (20)$$

the analytical solution is given by

$$\psi_{ab}^l(k+1) = \frac{|W_{ab}^l(k+1)|}{\omega_{ab}^l(k)}$$

where $\omega_{ab}^l(k) = \sqrt{\alpha_{ab}^l(k)}$.

For the second part, finding \mathcal{W} can be done with stochastic gradient descent on Eq. (14), which can be reformulated as a regularized loss function as follows:

$$\begin{aligned} \mathcal{W}(k+1) &= \underset{\mathcal{W}}{\operatorname{argmin}} \mathcal{W}^T \mathbf{H} \mathcal{W} + 2 \mathcal{W}^T \hat{\mathbf{g}} \\ &\quad + \sum_{l=1}^L \sum_{a=1}^{n_{l-1}} \sum_{b=1}^{n_l} \|\omega_{ab}^l \cdot W_{ab}^l\|_{l_1} \end{aligned} \quad (21)$$

$$\approx \underset{W}{\operatorname{argmin}} \mathbf{E}(\cdot) + \lambda \sum_{l=1}^L \rho(\omega^l, W^l). \quad (22)$$

$\mathbf{E}(\cdot)$ designates the energy loss function defined in Eq. (3) and $\rho(\cdot)$ the regularization term.

D. Hessian computation

The Hessian of the weight matrices is a required component for the Laplace approximation method. Previous works [1] and [9] have proposed the efficient recursive method to compute Hessian for a Fully-connected layer and convolutional layer, respectively. Inspired by these two works, we propose a recursive and efficient method to compute the Hessian of a recurrent layer.

A LSTM cell is a special form of the RNN. For the convenience of explanation, we use a simplified RNN structure to illustrate the Hessian calculation process. As shown in Fig 3, we denote $z(t)$, $h(t)$ and $y(t)$ as the input, hidden state and output of the time step t , respectively. The behavior of this RNN layer can be described by

$$h(t) = \sigma(W_i z(t) + W_h h(t-1)), \quad y(t) = W_o h(t) \quad (23)$$

where W_i , W_h and W_o represent the weight matrix of the input layer, hidden layer and output layer, respectively, and σ is the activation function. The Hessian should be

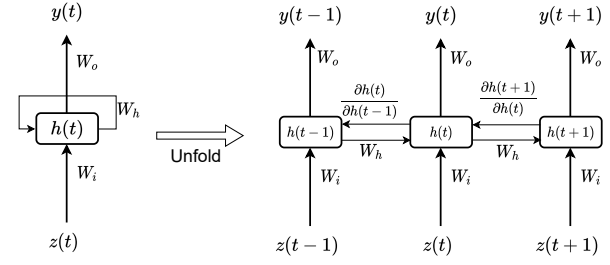


Fig. 3: An unrolled RNN layer.

calculated through a BPTT process. Refer to [1], the Hessian for W_o is:

$$\mathbf{H}_o = \frac{1}{T} \sum_{t=1}^T \mathbf{H}_o^t \quad (24)$$

where $\mathbf{H}_o^t = (h(t))^2 \otimes H_o^t$ and H_o^t is the pre-activation Hessian of W_o , with \otimes standing for Kronecker product. Suppose that τ is the backward propagation time horizon, then the Hessian of W_h is computed as:

$$\begin{aligned} \mathbf{H}_h &= \frac{1}{T \times \tau} \sum_{t=1}^T \sum_{j=t-\tau+1}^t \mathbf{H}_h^{t,j} \\ \mathbf{H}_h^{t,j} &= (z(t-1))^2 \otimes H_h^{t,j} \end{aligned} \quad (25)$$

where $\mathbf{H}_h^{t,j}$ and $H_h^{t,j}$ represent the Hessian and the pre-activation Hessian, respectively. In particular, $H_h^{t,j} = B^2 \odot (((W_h)^T)^2 H_h^{t,j+1}) + D$, where $B = \sigma'(h(t))$, $D = \sigma''(h(t)) \odot \frac{\partial L}{\partial h(t)}$. As the pre-activation Hessian H_h and Hessian \mathbf{H}_h will be imparted along with the backward propagation process over the time horizon τ , the Hessian of the W_i is:

$$\mathbf{H}_i = \frac{1}{T \times \tau} \sum_{t=1}^T \sum_{k=t-\tau+1}^t \mathbf{H}_i^{t,k} \quad (26)$$

where $\mathbf{H}_i^{t,k} = (z(k-1))^2 \otimes H_i^{t,k}$ with $H_i^{t,k} = \prod_{j=k+1}^t B^2 \odot (((W_i)^T)^2 H_i^{j,j-1})$.

IV. REGULARIZED IDENTIFICATION ALGORITHM

A. Input regressor selection and structured sparsity regularization

As illustrated in Section II-A, the input regressor is $z(t+1) = [u(t+1), u(t), \dots, u(t-l_u), y(t), y(t-1), \dots, y(t-l_y)]^\top \in \mathbb{R}^{l_u+l_y+1}$. The feature selection means to identify and remove the redundant features from $z(t+1)$. The proposed method can select the input regressors automatically by imposing structured sparsity regularization on the DNN.

Specifically, the iterative procedure derived in Section III includes an assumption on the independence and non-stationarity of connection weights, resulting in a shape-wise regularization as shown in Fig. 4(a). This drives individual connection weights to 0. In some applications, one may want to enforce more structured sparsity by pre-defining groups and re-expressing the regularization term as a function of these groups [9]. This paper uses a structured regularization of rows and columns (Fig. 4(b-d)). The benefits of such an approach, specific to this paper, are obtaining compact sparse models and the suppression of input nodes in z that are deemed less pertinent without loss of accuracy. The reduction in the dimensionality of the input vector z represents the selection of input regressors.

To extend this approach to the Bayesian framework, one has to revisit the prior formulation. The prior of a weight matrix is formulated based on the designated group of weight matrices (row or column or both). These groups are considered independent, but the connection weights of a specific group share the same prior Gaussian relaxation (see Fig. 4(b-d)). This results in a slightly different iterative update rule for the identification algorithm.

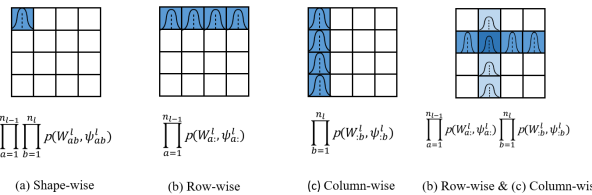


Fig. 4: Priors for structured sparsity of weight matrices.

For each of the cases shown in Fig. 4, the update rules for ψ , ω and the regularization function ρ are given in Appendix C Table II. There also stands more insights into how the adopted group priors slightly change the regularization update rules to group Lasso regularizers [28].

B. Algorithm

A pseudocode for the iterative procedure is given by Algorithm 1.

Remark 1: We now give some clarifications on the definition of cycle and epoch in Algorithm 1. One identification “cycle” has E_{\max} epochs. One “epoch” refers to that the entire dataset is processed forward and backward by the NN for one time. In the first identification cycle, the regularization is conventional ($\omega(0) = \mathbb{1}$). That is, the first obtained model is a sparse model corresponding to

Algorithm 1 Identification Algorithm

Input:

- Collect input-output data $u(t)$ and $y(t)$ for $t = 1, 2, \dots, T$.
- Arrange input regressors according to the chosen lags l_u, l_y .
- Set regularization parameter λ (empirically tuned) and DNN pruning thresholds κ_ψ, κ_W ($\approx 10^{-3}$).
- Set the number of repeated experiments M , identification cycles C_{\max} and the number of epochs in each cycle E_{\max} .
- Initialize hyper-parameters $\Psi(0) = \mathbf{I}$ and $\omega(0) = \mathbb{1}$.

Output: Return the set of connection weights \mathcal{W}

for $m = 1$ to M **do**

for $c = 1$ to C_{\max} **do**

for $e = 1$ to E_{\max} **do**

 1 Stochastic Gradient Descent with loss function (ρ is defined in Table II):

$$\mathcal{W}(k+1) = \min_{\mathcal{W}} \mathbf{L}(\cdot) + \lambda \sum_{i=1}^N \rho(\omega^i, W^i) \quad (27)$$

end for

 2 Update α according to Eqs. (17)-(18)

 3 Update ψ and ω according to Table II

 4 Dynamic pruning:

if $\psi_{ab}^l(k) < \kappa_\psi$ **or** $|W_{ab}^l(k)| < \kappa_W$ **then**

prune $W_{ab}^l(k)$

end if

end for

 Simulate on the validation data and choose the model with the smallest root mean square error (RMSE).

end for

the conventional sparse group lasso regularization method (as shown in (27)), and sparser models are expected to result from the next identification cycles.

Remark 2: The proposed algorithm shares the local convergence properties (local minima, saddle point) of the adopted stochastic gradient descent method [27]. This is because the Laplace approximation is a local approximation method and includes an assumption on the unimodality of the posterior. However, the pruning and regularization techniques introduced are heuristics that help speed up the algorithm and improve convergence and optimality. Nonetheless, the identification experiments are run multiple times with different initialization, and the identified model with the best simulation accuracy is chosen.

C. Making predictions with uncertainties

In the Bayesian procedure, predictions are made using the posterior predictive distribution, which is given by:

$$p(\hat{y}|z, \mathcal{D}) = \int p(\hat{y}|\mathcal{W}, z) p(\mathcal{W}|\mathcal{D}) d\mathcal{W}. \quad (28)$$

The first term of the integral is the likelihood of the prediction conditional on the network parameters. The second term is the inferred posterior distribution over the

weights \mathcal{W} given the training data \mathcal{D} . The expected value of the prediction is:

$$\mathbb{E}[\hat{y}] = \int \hat{y} p(\hat{y}|z, \mathcal{D}) d\hat{y} \quad (29)$$

$$= \int \left(\int \hat{y} p(\hat{y}|\mathcal{W}, z) d\hat{y} \right) p(\mathcal{W}|\mathcal{D}) d\mathcal{W} \quad (30)$$

$$= \int \text{Net}(\mathcal{W}, z) p(\mathcal{W}|\mathcal{D}) d\mathcal{W}. \quad (31)$$

Using the inferred posterior distribution over the weights, one can approximate this integral by Monte-Carlo sampling methods. An unbiased estimate of the prediction is given by the average predictions using \mathcal{W} sampled by the posterior M times as below:

$$\mu_{\hat{y}} \approx \frac{1}{M} \sum_{m=1}^M \text{Net}(\mathcal{W}(m), z). \quad (32)$$

In an analogous way, to estimate the variance in the posterior predictive distribution, the expected value $\mathbb{E}[\hat{y}^T \hat{y}]$ is analytically derived as follows:

$$\mathbb{E}[\hat{y}^T \hat{y}] = \int \hat{y}^T \hat{y} p(\hat{y}|z, \mathcal{D}) d\hat{y} \quad (33)$$

$$= \int \left(\int \hat{y}^T \hat{y} p(\hat{y}|\mathcal{W}, z) d\hat{y} \right) p(\mathcal{W}|\mathcal{D}) d\mathcal{W} \quad (34)$$

$$= \int (\theta + \text{Net}(\mathcal{W}, z)^2) p(\mathcal{W}|\mathcal{D}) d\mathcal{W}. \quad (35)$$

An unbiased estimate of the variance is given by Monte-Carlo integration methods [44], with M samples from the inferred posterior distribution of \mathcal{W} as below:

$$\Sigma_{\hat{y}} \approx \theta + \frac{1}{M} \sum_{m=1}^M \text{Net}(\mathcal{W}(m), z)^2 - \mu_{\hat{y}}^T \mu_{\hat{y}}. \quad (36)$$

This variance (Eq. (36)) represents the model uncertainty in the prediction. It is approximated by the sum of an aleatoric uncertainty and epistemic uncertainty. The aleatoric uncertainty is generally known to be irreducible corresponding to the noise covariance of the measurement and is generally incorporated in the likelihood form [44]. For example, if the likelihood is given as Gaussian distribution, then θ should represent the noise variance. The epistemic uncertainty corresponds to the model's uncertainty in a prediction that is often called reducible uncertainty [44] and grows when moving away from the training data [4].

D. Validation and software implementation

The identification experiments are implemented using the PyTorch library[‡]. The MLP and LSTM models are randomly initialized, trained based on a one-step-ahead prediction approach, and validated based on a free run simulation setting. The stochastic gradient descent method adopted is the ADAM optimizer, and the learning rate is scheduled using Cosine Annealing for each identification experiment.

For the evaluation metric, it should be noted that prediction and simulation error are two typical evaluation metrics for SYSID. Given the current and past measurements

of the system input and output, the prediction means predicting the system response to the future k steps, where k denotes the prediction horizon. Simulation is to predict the system response based only on the input data and initial conditions. Therefore, the simulation error is a more challenging evaluation metric and is used in this paper. The figure of merit used is given by the root mean square error (RMSE) of the simulation experiment:

$$RMSE(\hat{y}, y) = \sqrt{\frac{1}{T} \sum_{i=1}^T (y_i - \hat{y}_i)^2}$$

V. EXPERIMENTS

An overview of the simulation accuracy of our experiments compared with other methods can be found in Tables III-IV in Appendix D.

A. Dataset and experiment setup

This section is to summarize the identification experiments of three linear processes and two nonlinear processes using the proposed algorithm. For linear systems, the identification procedure is repeated $M = 20$ times with $C_{\max} = 6$ identification cycles. For nonlinear systems, the identification is also repeated $M = 20$ times but with $C_{\max} = 10$ identification cycles each. Table I provides a summary of the model structure used for identification as well as the mean, standard deviation, and minimum validation RMSE of the M best-identified models and the percentage of sparse parameters in the best-identified model. In Appendix E-Appendix I, the benchmarks are described more thoroughly with sparsity plots, simulation plots, and plots of posterior predictive mean and uncertainty corresponding to the best-identified model.

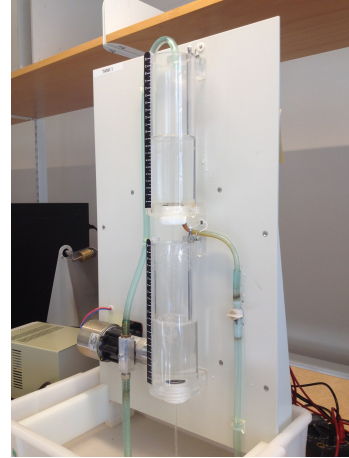


Fig. 5: The cascaded tanks setup [26].

Three linear processes are identified, the Hairdryer, Heat exchanger and Glass Tube (GT) manufacturing process. The datasets of these processes are provided by Matlab in the corresponding tutorials (<https://nl.mathworks.com/help/ident/examples.html>) on linear SYSID. The chosen best validated models are compared to the methods used in the corresponding tutorials. Additional model structures used for the identification of the Hairdryer are taken from Chapter 17.3 of [18] and run in Matlab. The comparisons are in Appendix D Table III.

[‡]<https://pytorch.org/>

TABLE I: Models are trained to identify linear and nonlinear processes with validation information

Process-Model	Layers-Units	Lags	RMSE _{val} ($\mu \pm \sigma$)	RMSE _{val} (min)	Sparsity	Appendix
Hairdryer-MLP	1 - 50	5	0.074 ± 0.0005	0.073	88.1%	Appendix E
Hairdryer-LSTM	1 - 10	5	0.093 ± 0.0166	0.081	93.5%	Appendix E
Heat Exchanger-MLP	1 - 50	150	0.086 ± 0.0002	0.086	99.3%	Appendix F
Heat Exchanger-LSTM	1 - 10	150	0.114 ± 0.0299	0.088	96.4%	Appendix F
GT Manufacturing-MLP	1 - 50	5	0.660 ± 0.0013	0.657	97.8%	Appendix G
GT Manufacturing-LSTM	1 - 10	5	0.671 ± 0.0019	0.669	99.0%	Appendix G
Cascaded Tanks-MLP	3 - 10	20	0.428 ± 0.1032	0.257	84.5%	Appendix H
Cascaded Tanks-LSTM	1 - 50	20	0.500 ± 0.1012	0.362	60.3%	Appendix H
CED-MLP	2 - 50	10	0.187 ± 0.0285 0.134 ± 0.0192	0.149 0.120	78.4%	Appendix I
CED-LSTM	1 - 10	10	0.155 ± 0.0257 0.126 ± 0.0201	0.121 0.097	72.8%	Appendix I

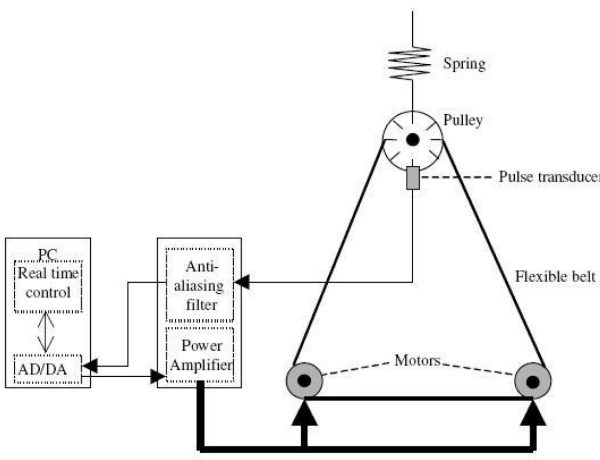


Fig. 6: The coupled electric drives setup [38].

Two nonlinear processes, the Cascaded Tanks [26], Coupled Electric Drives [38] are also identified. Information and datasets of these benchmarks are compiled in the web page of the Workshop on Nonlinear System Identification Benchmarks (<https://sites.google.com/view/nonlinear-benchmark/>). The cascaded tank system is a fluid level control system, which is consist of two tanks with free outlets fed by a water pump [26]. The fluid levels of these two tanks are adjusted by the input signal that controls the water pump. The setup of the cascaded tanks is shown in Fig 5. The coupled electric drives is a system that drives a pulley by controlling a flexible belt. Two electric motors provide the driving force, and the spring is used to fix the pulley. The setup of the Coupled Electric Drives is shown in Fig. 6. A more detailed description of the system and datasets of these benchmarks are compiled on the web page of the Nonlinear System Identification Benchmarks. The models with the best validation performance are compared with best models obtained using conventional NN methods for multiple experiments ($M = 20$) and the previous works in the literature for every benchmark in Appendix D Table IV.

B. Analysis on experimental results

In this subsection, the results will be discussed and analyzed in relation to the claims made on sparsity, uncertainty quantification, and simulation accuracy.

Sparsity: In most cases, the obtained networks are sparse models with structured sparsity, for example, Fig 7 is a sparsity plot of the Heat Exchanger identified LSTM Model. According to Table I, sparsity is more prominent in the identified linear systems than in nonlinear systems. This demonstrates that the nonlinearity that the data exhibits requires a higher complexity than in the linear case.

Starting with the linear systems, one can note that structured sparsity induced a recognized transport delay in the Heat Exchanger MLP and LSTM models, which characterizes this system. Furthermore, the LSTM models for linear systems have complete operators pruned. This means that the cell state can be well regulated with fewer parameters than imposed by the initialized model structure in the Heat Exchanger case. Similar behavior is seen across linear benchmarks.

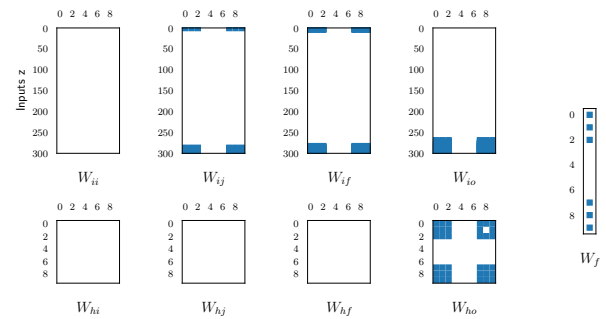


Fig. 7: Sparsity plot of the identified LSTM for Heat Exchanger. (Blue represents non-pruned connection weights)

Structured sparsity is also observed in the identified networks for nonlinear systems (Table I). In addition to that, similar to LSTM models identified for linear systems, a lot of parameters involving the hidden states are pruned. A possible explanation for this behavior is that the hidden states of LSTM units attempt to retain short-term information from the time series that is also available as lagged elements in the input regressor. The simulation

result further shows that the input regressor with lagged elements can achieve better simulation performance for a LSTM model (see Appendix D Table III-IV). Another observation related to the structured sparsity regularization is the effect of input regressor selection. As shown in Fig. 15a in Appendix G, the number of input regressors is reduced from 40 to 2 after applying the sparse Bayesian algorithm with row-wise and column-wise prior as shown in Appendix C Table II. The redundant input regressors are also identified for other benchmarks and removed from the NN, thereby reducing the model complexity.

We also find that DNNs (MLP models) with more hidden layers are necessities to approximate complex systems. For example, the optimal MLP model of the nonlinear cascaded tanks system includes three hidden layers, while the optimal MLP model of the linear hairdryer system only has one hidden layer. The MLP model with only one hidden layer and 10 hidden neurons is also applied for the cascaded tank system. However, the obtained simulation error is around 0.663, which is worse than the MLP model with three hidden layers (0.257 as in Table I). It should also be noted that although the number of hidden layers of the MLP models is not reduced in these experiments, the number of hidden neurons is reduced, which provides a more suitable network structure for different systems. For example, as shown in Fig. 13a, the number of hidden neurons in the MLP model of the Heat Exchanger model is reduced from 50 to 7.

Predictive distributions: The posterior predictive distributions for each model result from the forward propagation of the parameters' posterior uncertainty obtained with the estimation data. Hence, if the validation data holds information that the model does not learn from the estimation data, then the posterior predictive distribution could spread a bigger range of predictions [4].

In some cases, the identified models show an unevenly distributed predictive uncertainty related to nonlinearities or disturbances characteristics of the process and regions where the model can be improved. Fig. 8 shows that the identified model for Cascaded Tanks makes less robust predictions when overflow occurs. The Heat Exchanger shows evenly distributed predictions with uncertainty possibly coming from the ambient temperature disturbance. Furthermore, the model type also affects the predictive distribution. Examples include the LSTM models identified for the Glass Tube Manufacturing Process and Cascaded Tanks. In these benchmarks, the identified MLP model provides more robust predictions than the identified LSTM model.

Free run simulation performance: The free run simulation is a good measure of the model's approximation ability to represent a dynamic process by propagating a model's prediction error while forecasting. In this paper, we select the simulation error as the evaluation metric. It is important to note that, for the studied linear processes, a non-regularized LSTM performs worse when compared to other identification methods. This supports the previous concerns made on using LSTM for the identification of linear systems. The Bayesian MLP model outperforms the Bayesian LSTM model in most presented applications except for the Coupled Electric Drive.

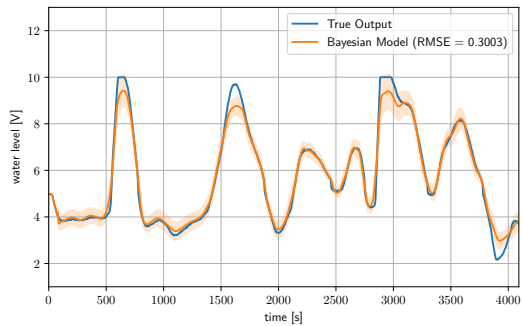


Fig. 8: Posterior predictive $\mu_y \pm 2\sigma_y$ of the identified LSTM on Cascaded Tanks benchmark.

Table I displays the mean and standard deviation of the validation simulation errors and the minimum corresponding to the best-chosen model. The minimum is seen to fall close to the range of one standard deviation from the mean. In addition, the variance of validation errors for linear systems is overall less than nonlinear systems. A possible explanation is that the added complexity in identifying nonlinear processes and the usage of more complex nonlinear structures (LSTM in this case), increases the likelihood of convergence towards saddle points. This is mainly because the Laplace method adopted is a local approximation of the evidence, which is a limitation of the proposed method and justifies running the identification experiment M times.

The Bayesian approach to the identification of each benchmark constitutes an improvement over the conventional MLP and LSTM methods in simulation errors and pushes these methods to perform competitively with other literature (see Table III-IV). Besides, we also make a comparison with the well-known Gaussian process (GP) in machine learning, by exploring different kernels (i.e., squared exponential kernel, rational quadratic kernel). However, GP method cannot perform input regressor selection efficiently, i.e., all regressors flow into the black box model without any priority. The detailed result of GP is put in Appendix D Table III-IV.

VI. CONCLUSION

In this paper, we have combined sparse Bayesian learning and deep learning for SYSID. An iterative procedure for dynamic SYSID has been derived and evaluated with datasets of three linear and two nonlinear dynamic processes. The Bayesian approach in this paper has used the Laplace approximation to approximate the model evidence/marginal likelihood. The structured sparsity regularization has been implemented on NNs by enforcing group-sparsity inducing priors. The identified models for the dynamic systems are sparse models that have contributed to input regressor selection and performed competitively with other used SYSID methods in a free run simulation setting. In addition, uncertainties in the inferred predictions and connection weights have been quantified using Monte-Carlo integration methods.

VII. FURTHER DISCUSSION

Regularization parameter λ in Algorithm 1: The regularization parameter λ in (27) needs to be tuned many times for network training, especially when using the simulation error as the evaluation metric. As a well-established strategy for global optimization, Bayesian optimization is a promising method that can alleviate the heavy tuning burden. A scalable Bayesian optimization method based on DNNs was proposed in [14]. A Bayesian optimization framework for DNN compression was also discussed in [43]. In the future, the application of Bayesian optimization in SYSID to reduce the hyper-parameter tuning burden is a research topic worthy of study.

Identification with physical interpretability: As explained in Section V-B, good and competitive simulation accuracy can be achieved across the five benchmark datasets. However, the identified NNs are still black-box models, which lack interpretability in physics and cannot provide understanding of the underlying phenomenon of the system. Recently, several methods have been proposed to identify governing equations. To name a few, a framework to identify the governing interactions and transition logics of subsystems in cyber-physical systems was developed in [46]. A practical sparse Bayesian approach was proposed in [41] to perform the online selection for the Hill function of synthetic gene networks. In [35], the sparse identification of nonlinear dynamics (SINDy) algorithm was proposed to identify the fewest equation terms that can describe a system. However, these approaches suffer from the nontrivial task of choosing appropriate basis functions, thereby limiting their capacity for more general applications. Inspired by the research of physics-informed machine learning [15] and symbolic regression, the problem of identifying system equations can be solved by designing a novel network structure with basic mathematical operations or encoding the prior information in the loss function.

Convergence of DNN training: The convergence of NN training is difficult to analyze, which is influenced by many aspects, i.e., the pre-processing of training data [34], the initialization of weight matrices [27], proper selection of learning rate and batch size, and the complexity of NN [27], [34]. A local convergence theory was developed for mildly over-parameterized two-layer NN, which shows the gradient descent can converge to zero with the initial loss below a threshold in [27]. [37] proposed to use the efficient conjugate gradient (CG) algorithm to train the RNN, which can accelerate the convergence procedure and help to find the optimal solution. In this paper, although there is no guarantee that the absolute global minimum can be achieved during the training process, the experimental result shows that the convergence trend is noticeable. This is also consistent with the research findings in [34] that state that the backpropagation process can always make it possible to meet practical stopping criteria.

APPENDIX A THE LAPLACE APPROXIMATION

In this section, a more detailed mathematical description of the Laplace approximation adopted is made. The

likelihood is given by an exponential family distribution as (3) in Section III-A. As a typical exponential family distribution, Gaussian distribution will be adopted in the following to show how to derive the iterative procedures. The formulation of the likelihood with Gaussian distribution is rewritten as:

$$\begin{aligned} p(\mathcal{D}|\mathcal{W}, \sigma^2) &= \prod_{t=1}^T \mathcal{N}(y(t)|\text{Net}(z(t), \mathcal{W}), \sigma^2) \\ &= (2\pi\sigma^2)^{-\frac{T}{2}} \exp \left\{ -\mathbf{L}(\mathcal{W}, \sigma^2) \right\}. \end{aligned}$$

$\mathbf{L}(\mathcal{W}, \sigma^2)$ is denoted as the energy function, or the loss of the network given the data \mathcal{D} . It is given by $\mathbf{L}(\mathcal{W}, \sigma^2) = \frac{1}{2\sigma^2} \sum_{t=1}^T (y(t) - \text{Net}(z(t), \mathcal{W}))^2$. The expression $\text{Net}(\cdot)$ is the resulting network nonlinear map. To compute the intractable integral for the evidence, the energy function can be expanded by using a second order Taylor series expansion around \mathcal{W}^* as follows:

$$\begin{aligned} \mathbf{E}(\mathcal{W}, \sigma^2) &\approx \mathbf{L}(\mathcal{W}^*, \sigma^2) + (\mathcal{W} - \mathcal{W}^*)^T \mathbf{g}(\mathcal{W}^*, \sigma^2) \\ &\quad + \frac{1}{2} (\mathcal{W} - \mathcal{W}^*)^T \mathbf{H}(\mathcal{W}^*, \sigma^2) (\mathcal{W} - \mathcal{W}^*) \end{aligned}$$

where $\mathbf{g} = \nabla \mathbf{E}(\mathcal{W}, \sigma^2)|_{\mathcal{W}^*}$ and $\mathbf{H} = \nabla \nabla \mathbf{E}(\mathcal{W}, \sigma^2)|_{\mathcal{W}^*}$. To ease notation, we use \mathbf{g} and \mathbf{H} to denote $\mathbf{E}(\mathcal{W}^*, \sigma^2)$ and $\mathbf{H}(\mathcal{W}^*, \sigma^2)$, respectively. The quadratic expression is also adopted among Trust-Region methods, where a region is defined around the current iterate connection weights \mathcal{W} and the expansion is considered as a reasonable local representation of the loss function. With this expansion, the likelihood function becomes:

$$p(\mathcal{D}|\mathcal{W}, \sigma^2) \approx \mathbf{A} \cdot \exp \left\{ -\left(\frac{1}{2}\mathcal{W}^T \mathbf{H} \mathcal{W} + \mathcal{W}^T \hat{\mathbf{g}}\right) \right\} \quad (37)$$

with $\hat{\mathbf{g}} = \mathbf{g} - \mathbf{H} \mathcal{W}^*$, $\mathbf{A} = (2\pi\sigma^2)^{-\frac{T}{2}} \cdot \exp \left\{ -\left(\frac{1}{2}\mathcal{W}^{*T} \mathbf{H} \mathcal{W}^* - \mathcal{W}^{*T} \mathbf{g} + \mathbf{L}(\mathcal{W}^*, \sigma^2)\right) \right\}$. A Gaussian form can be easily recuperated from (37) by completing the square in the exponent. Before that, we define the following quantities: $\mathbf{B} = \exp \left\{ \frac{1}{2} \hat{\mathbf{g}}^T \mathbf{H} \hat{\mathbf{g}} \right\}$ and $\mathbf{C} = (2\pi)^{\frac{\kappa}{2}} |\mathbf{H}|^{\frac{1}{2}}$ then (37) can be reformulated as:

$$\begin{aligned} p(\mathcal{D}|\mathcal{W}, \sigma^2) &\approx \mathbf{A} \cdot \exp \left\{ -\left(\frac{1}{2}\mathcal{W}^T \mathbf{H} \mathcal{W} + \mathcal{W}^T \hat{\mathbf{g}}\right) \right\} \\ &\quad \cdot \exp \left\{ \frac{1}{2} \hat{\mathbf{g}}^T \mathbf{H} \hat{\mathbf{g}} - \frac{1}{2} \hat{\mathbf{g}}^T \mathbf{H} \hat{\mathbf{g}} \right\} \\ &= \mathbf{A} \cdot \mathbf{B} \cdot \exp \left\{ -\left(\frac{1}{2}\mathcal{W}^T \mathbf{H} \mathcal{W} + \mathcal{W}^T \hat{\mathbf{g}} + \frac{1}{2} \hat{\mathbf{g}}^T \mathbf{H} \hat{\mathbf{g}}\right) \right\} \\ &= \mathbf{A} \cdot \mathbf{B} \cdot \mathbf{C} \cdot \mathcal{N}(\mathcal{W}|\hat{\mathcal{W}}, \mathbf{H}^{-1}) \end{aligned}$$

where $\hat{\mathcal{W}} = -\mathbf{H}^{-1} \hat{\mathbf{g}}$. Given a Gaussian likelihood and a Gaussian prior defined in Section II-B, by effect of the conjugacy rule, the posterior is also Gaussian $\mathcal{N}(\mu_{\mathcal{W}}, \Sigma_{\mathcal{W}})$ with $\mu_{\mathcal{W}} = [\mathbf{H} + \Psi^{-1}]^{-1} \hat{\mathbf{g}}$ and $\Sigma_{\mathcal{W}} = [\mathbf{H} + \Psi^{-1}]^{-1}$.

APPENDIX B EVIDENCE MAXIMIZATION

This section provides a mathematical proof of the derived objective function. Starting from the maximization

in Eq. (4), the likelihood and prior are replaced by their expressions in the preliminary Section II-B. Then we have

$$\begin{aligned}
& \int p(\mathcal{D}|\mathcal{W}, \sigma^2) p(\mathcal{W}|\psi) p(\psi) d\mathcal{W} \\
&= \int \mathbf{A} \cdot \exp \left\{ - \left(\frac{1}{2} \mathcal{W}^T \mathbf{H} \mathcal{W} + \mathcal{W}^T \hat{\mathbf{g}} \right) \right\} \\
&\quad \cdot \mathcal{N}(\mathcal{W}|0, \Psi) \cdot \phi(\psi) d\mathcal{W} \\
&= \frac{\mathbf{A}}{(2\pi)^{K/2} |\Psi|^{\frac{1}{2}}} \cdot \int \exp \left\{ - \left(\frac{1}{2} \mathcal{W}^T \mathbf{H} \mathcal{W} + \mathcal{W}^T \hat{\mathbf{g}} \right) \right\} \\
&\quad \cdot \exp \left\{ - \left(\frac{1}{2} \mathcal{W}^T \Psi^{-1} \mathcal{W} \right) \right\} d\mathcal{W} \cdot \prod_{l=1}^L \prod_{a=1}^{n^{l-1}} \prod_{b=1}^{n^l} \phi(\psi_{ab}^l) \\
&= \frac{\mathbf{A}}{(2\pi)^{K/2} |\Psi|^{\frac{1}{2}}} \cdot \int \exp \left\{ - \mathcal{E}(\mathcal{W}, \sigma^2) \right\} d\mathcal{W} \\
&\quad \cdot \prod_{l=1}^L \prod_{a=1}^{n^{l-1}} \prod_{b=1}^{n^l} \phi(\psi_{ab}^l)
\end{aligned}$$

where $\mathcal{E}(\mathcal{W}, \sigma^2) = \frac{1}{2} \mathcal{W}^T \mathbf{H} \mathcal{W} + \mathcal{W}^T \hat{\mathbf{g}} + \frac{1}{2} \mathcal{W}^T \Psi^{-1} \mathcal{W}$. The integral in Eq. (38) is the integral of the product $p(\mathcal{D}|\mathcal{W}, \sigma^2) p(\mathcal{W}|\psi)$, which is proportional to the posterior $p(\mathcal{W}|\mathcal{D}, \psi)$. In most applications, the posterior peaks with respect to the prior, and the evidence can be approximated by the posterior volume. This approximation is analogous to the usage of the Laplace approximation of the posterior in David MacKay's Bayesian framework [20]. That is,

$$\begin{aligned}
& \int p(\mathcal{D}|\mathcal{W}, \sigma^2) p(\mathcal{W}|\psi) d\mathcal{W} \\
&\approx p(\mathcal{D}|\mu_{\mathcal{W}}, \sigma^2) p(\mu_{\mathcal{W}}|\psi) \cdot |\Sigma_{\mathcal{W}}|^{\frac{1}{2}} \cdot (2\pi)^{\kappa/2} \\
&\iff \int \exp \left\{ - \mathcal{E}(\mathcal{W}, \sigma^2) \right\} d\mathcal{W} \\
&\approx \exp \left\{ - \mathcal{E}(\mu_{\mathcal{W}}, \sigma^2) \right\} \cdot |\Sigma_{\mathcal{W}}|^{\frac{1}{2}} \cdot (2\pi)^{\kappa/2}
\end{aligned} \tag{38}$$

where

$$\begin{aligned}
\mathcal{E}(\mu_{\mathcal{W}}, \sigma^2) &= \frac{1}{2} \mu_{\mathcal{W}}^T \mathbf{H} \mu_{\mathcal{W}} + \mu_{\mathcal{W}}^T \hat{\mathbf{g}} + \frac{1}{2} \mu_{\mathcal{W}}^T \Psi^{-1} \mu_{\mathcal{W}} \\
&= \min_{\mathcal{W}} \frac{1}{2} \mathcal{W}^T \mathbf{H} \mathcal{W} + \mathcal{W}^T \hat{\mathbf{g}} + \frac{1}{2} \mathcal{W}^T \Psi^{-1} \mathcal{W}.
\end{aligned} \tag{39}$$

Hence, the maximization of the evidence becomes the maximization below:

$$\begin{aligned}
\psi &= \operatorname{argmax}_{\psi > 0} \frac{\mathbf{A}}{(2\pi)^{\kappa/2} |\Psi|^{\frac{1}{2}}} \cdot \exp \left\{ - \mathcal{E}(\mu_{\mathcal{W}}, \sigma^2) \right\} \\
&\quad \cdot |\Sigma_{\mathcal{W}}|^{\frac{1}{2}} \cdot \prod_{l=1}^L \prod_{a=1}^{n^{l-1}} \prod_{b=1}^{n^l} \phi(\psi_{ab}^l).
\end{aligned}$$

By applying a $-2 \log(\cdot)$ operation and using Eq. (39), one obtains

$$\begin{aligned}
\psi &= \operatorname{argmin}_{\psi > 0} -2 \log \left[\frac{\mathbf{A} \cdot \exp \left\{ - \mathcal{E}(\mu_{\mathcal{W}}, \sigma^2) \right\}}{(2\pi)^{\kappa/2} |\Psi|^{\frac{1}{2}}} \right. \\
&\quad \cdot |\Sigma_{\mathcal{W}}|^{\frac{1}{2}} \cdot \prod_{l=1}^L \prod_{a=1}^{n^{l-1}} \prod_{b=1}^{n^l} \phi(\psi_{ab}^l) \left. \right] \\
&= \operatorname{argmin}_{\psi > 0} -2 \log(\mathbf{A}) + \mathcal{E}(\mu_{\mathcal{W}}, \sigma^2) + \log |\Psi| \\
&\quad - \log |\Sigma_{\mathcal{W}}| - 2 \sum_{l=1}^L \sum_{a=1}^{n^{l-1}} \sum_{b=1}^{n^l} \log(\phi(\psi_{ab}^l)) \\
\mathcal{W}, \psi &= \operatorname{argmin}_{\mathcal{W}, \psi > 0} \frac{1}{2} \mathcal{W}^T \mathbf{H} \mathcal{W} + \mathcal{W}^T \hat{\mathbf{g}} + \frac{1}{2} \mathcal{W}^T \Psi^{-1} \mathcal{W} \\
&\quad + \log |\Psi| + \log |\mathbf{H} + \Psi^{-1}| - 2 \log(\mathbf{A}) \\
&\quad - 2 \sum_{l=1}^L \sum_{a=1}^{n^{l-1}} \sum_{b=1}^{n^l} \log(\phi(\psi_{ab}^l)).
\end{aligned}$$

Since the hyperprior $\phi(\psi)$ is a non-informative hyperprior, the final objective function is given by:

$$\begin{aligned}
\mathcal{L}(\mathcal{W}, \psi, \sigma^2) &= \mathcal{W}^T \mathbf{H} \mathcal{W} + 2 \mathcal{W}^T \hat{\mathbf{g}} + \mathcal{W}^T \Psi^{-1} \mathcal{W} \\
&\quad + \log |\Psi| + \log |\mathbf{H} + \Psi^{-1}| - T \log(2\pi\sigma^2).
\end{aligned}$$

APPENDIX C REGULARIZATION UPDATE RULES

To enforce a group regularization on network parameters, the prior formulation is revisited, which does not alter the derivation of the loss function. The difference is with the optimization step for ψ . Parameters in the same row share the prior uncertainty parameter ψ_a^l , and in the same column the prior uncertainty ψ_b^l . The optimization step in Eq. (19) for ψ_b^l , the prior width shared among the connection weights in the same column, becomes

$$\psi_b^l(k+1) = \operatorname{argmin}_{\psi \geq 0} \sum_{b=1}^{n^l} \frac{W_{:b}^l(k+1)^T W_{:b}^l(k+1)}{\psi} + \alpha_{:b}^l(k) \cdot \psi \tag{40}$$

where $\alpha_{:b}^l = \sum_{a=1}^{n^{l-1}} \alpha_{ab}^l(k)$. By noting that

$$\sum_{b=1}^{n^l} \frac{W_{:b}^l T W_{:b}^l}{\psi} + \alpha_{:b}^l \cdot \psi \geq 2 \left\| \sqrt{\alpha_{:b}^l} \cdot W_{:b}^l \right\|_{l_2} \tag{41}$$

the analytical solution is given by $\psi_{:b}^l(k+1) = \frac{||W_{:b}^l(k+1)||_2}{\omega_{:b}^l(k)}$ where $\omega_{:b}^l(k) = \sqrt{\alpha_{:b}^l(k)} = \sqrt{\sum_{a=1}^{n^{l-1}} \alpha_{ab}^l(k)}$.

The row-wise regularization can be analogously derived. Note that the update rules for α_{ab}^l remains similar to Eq. (17) and (18). However, when using both row-wise and column-wise group regularization, the posterior is updated according to a combined prior expressed with a prior width given by :

$$\psi_{ab}^l(k) = \frac{1}{\left(\frac{1}{\psi_{a:}^l(k)} + \frac{1}{\psi_{:b}^l(k)} \right)}. \tag{42}$$

Table II summarizes the update rules according to the category of regularization techniques adopted.

TABLE II: Hyper-parameters update rule based on regularization technique.

Category	Prior Formulation	$\rho(\omega^l, W^l)$	ω^l	ψ^l
(a) Shape-wise	$\prod_{a=1}^{n_l-1} \prod_{b=1}^{n_l} p(W_{ab}^l, \psi_{ab}^l)$	$\sum_{a=1}^{n_l-1} \sum_{b=1}^{n_l} \ \omega_{ab}^l(k) \cdot W_{ab}^l(k)\ _{l_1}$	$\omega_{ab}^l(k) = \sqrt{\alpha_{ab}^l(k)}$	$\psi_{ab}^l(k) = \frac{ W_{ab}^l(k) }{\omega_{ab}^l(k-1)}$
(b) Row-wise	$\prod_{a=1}^{n_l-1} p(W_{a:}^l, \psi_{a:}^l)$	$\sum_{a=1}^{n_l-1} \ \omega_{a:}^l(k) \cdot W_{a:}^l(k)\ _{l_2}$	$\omega_{a:}^l(k) = \sqrt{\sum_{b=1}^{n_l} \alpha_{ab}^l(k)}$	$\psi_{a:}^l(k) = \frac{\ W_{a:}^l(k)\ _2}{\omega_{a:}^l(k-1)}$
(c) Column-wise	$\prod_{b=1}^{n_l} p(W_{:b}^l, \psi_{:b}^l)$	$\sum_{b=1}^{n_l} \ \omega_{:b}^l(k) \cdot W_{:b}^l(k)\ _{l_2}$	$\omega_{:b}^l(k) = \sqrt{\sum_{a=1}^{n_l-1} \alpha_{ab}^l(k)}$	$\psi_{:b}^l(k) = \frac{\ W_{:b}^l(k)\ _2}{\omega_{:b}^l(k-1)}$
(b) Row-wise + (c) Column-wise	$\prod_{a=1}^{n_l-1} p(W_{a:}^l, \psi_{a:}^l)$ $\times \prod_{b=1}^{n_l} p(W_{:b}^l, \psi_{:b}^l)$	$\sum_{a=1}^{n_l-1} \ \omega_{a:}^l(k) \cdot W_{a:}^l(k)\ _{l_2}$ $+ \sum_{b=1}^{n_l} \ \omega_{:b}^l(k) \cdot W_{:b}^l(k)\ _{l_2}$	$\omega_{a:}^l(k) = \sqrt{\sum_{b=1}^{n_l} \alpha_{ab}^l(k)}$ $\omega_{:b}^l(k) = \sqrt{\sum_{a=1}^{n_l-1} \alpha_{ab}^l(k)}$	$\psi_{a:}^l(k) = \frac{\ W_{a:}^l(k)\ _2}{\omega_{a:}^l(k-1)}$ $\psi_{:b}^l(k) = \frac{\ W_{:b}^l(k)\ _2}{\omega_{:b}^l(k-1)}$ $\psi_{ab}^l(k) = 1 / \left(\frac{1}{\psi_{a:}^l(k)} + \frac{1}{\psi_{:b}^l(k)} \right)$

APPENDIX D FREE RUN SIMULATION RESULTS

As shown in Fig. 9 and Table III and IV, this appendix includes the plots of the simulated experiments using the models identified and a comparison with previous models used in literature. The details of experiment settings on each benchmark are given in following sections (see Section E–Section I).

TABLE III: Comparison of RMSE on identified linear systems with other works

Appliance	RMSE [V]
Transfer Function Estimation [10]	0.108
Subspace Identification [18]	0.105
ARMAX Model [18]	0.104
ARX Model [18]	0.103
GPA ^a with rational quadratic kernel	0.066
GPA ^a with squared exponential kernel	0.066
LSTM without lags	0.219
LSTM without regularization	0.205
Bayesian LSTM	0.081
MLP without regularization	0.076
Bayesian MLP	0.073
Heat Exchanger	RMSE [°C]
Transfer Function Estimation [11]	0.140
Process and Disturbance Model [11]	0.089
Process Model [11]	0.088
GPA ^a with rational quadratic kernel	0.187
GPA ^a with squared exponential kernel	0.187
LSTM without lags	0.185
LSTM without regularization	0.158
Bayesian LSTM	0.088
MLP without regularization	0.092
Bayesian MLP	0.086
Glass Tube Manufacturing	RMSE [-]
Subspace Identification [12]	0.688
ARX Model [12]	0.676
GPA ^a with rational quadratic kernel	0.654
GPA ^a with squared exponential kernel	0.656
LSTM without lags	1.099
LSTM without regularization	1.056
Bayesian LSTM	0.669
MLP without regularization	0.663
Bayesian MLP	0.657

APPENDIX E HAIRDRYER

In common industrial settings with heating, temperature control is a highly desired objective given the high transport lags and process delay. The “hairdryer” is a small scale laboratory apparatus that designates the PT326 process trainer [11]. A mass of air is heated with thermal

TABLE IV: Comparison of RMSE on identified nonlinear systems with other works

Cascaded Tanks	RMSE [V]
LMN ^b with NFIR [13]	0.669
Flexible State Space Model [5]	0.450
Volterra Feedback Model [25]	0.397
OEM ^c with NOMAD [21]	0.376
Piecewise ARX Models [29]	0.350
NLSS ^d [31]	0.343
Tensor network B-splines [30]	0.302
GPA ^a with rational quadratic kernel	0.344
GPA ^a with squared exponential kernel	0.344
LSTM without lags	0.954
LSTM without regularization	0.494
Bayesian LSTM	0.362
MLP without regularization	0.432
Bayesian MLP	0.257
Coupled Electric Drives	RMSE [ticks/s]
	Drive 1 Drive 2
Extended Fuzzy Logic [32]	0.150 0.092
Cascaded Splines [24]	0.216 0.110
TAG3PD ^e [33]	- 0.128
RBFNN - FSDE ^f [8]	0.130 0.185
GPA ^a with rational quadratic kernel	0.150 0.167
GPA ^a with squared exponential kernel	0.153 0.132
LSTM without lags	0.394 0.252
LSTM without regularization	0.149 0.131
Bayesian LSTM	0.121 0.097
MLP without regularization	0.206 0.111
Bayesian MLP	0.149 0.120

^a Gaussian process model.

^b Tree based Local Model Networks with external dynamics represented by NARX or NFIR.

^c Output Error parametric Model estimation based on derivative free method.

^d nonlinear State Space model.

^e Tree Adjoining Grammars

^f Free Search Differential Evolution is used to determine the regressors.

resistors and flows in a tube. The temperature at the outlet is measured by a thermocouple in volts. The objective is to identify the dynamic relationship between the input voltage to the thermal resistors and the thermocouple voltage at the outlet. The dataset specific to this device is given by MATLAB in a tutorial on linear system identification. The sampling time is 0.08 seconds and the dataset contains 1000 data points. The dataset is detrended, bringing data to a zero mean. The first 300 data points are used for identification and the remaining 700 are used for validation.

A fully connected MLP model with one hidden layer and 50 nodes is randomly initialized. The activation function is a linear activation without the bias term. The

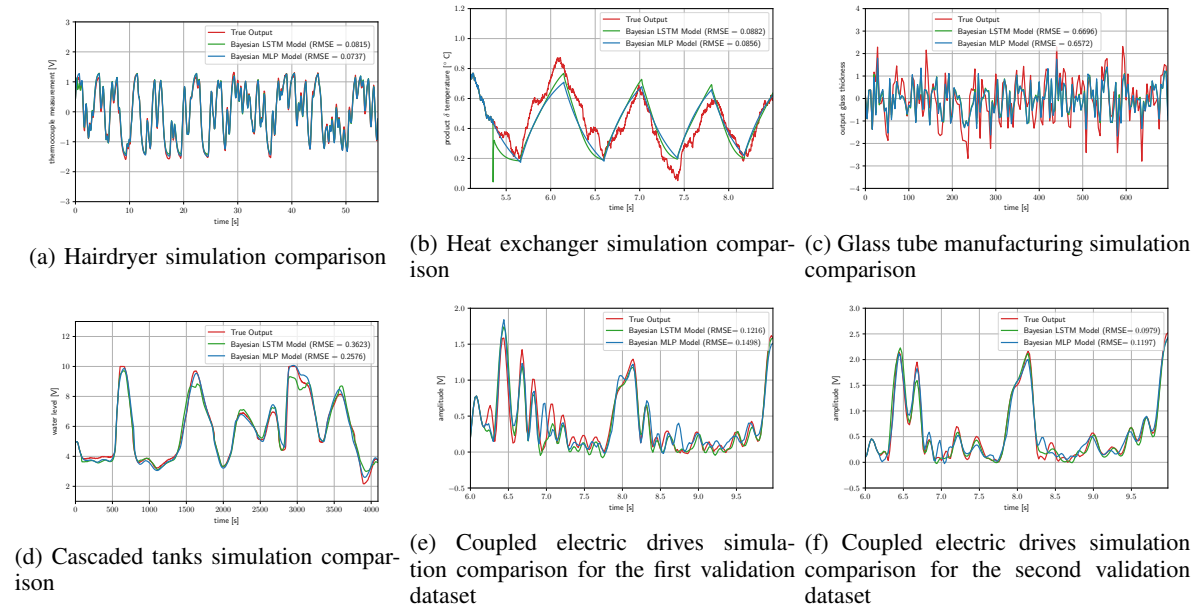
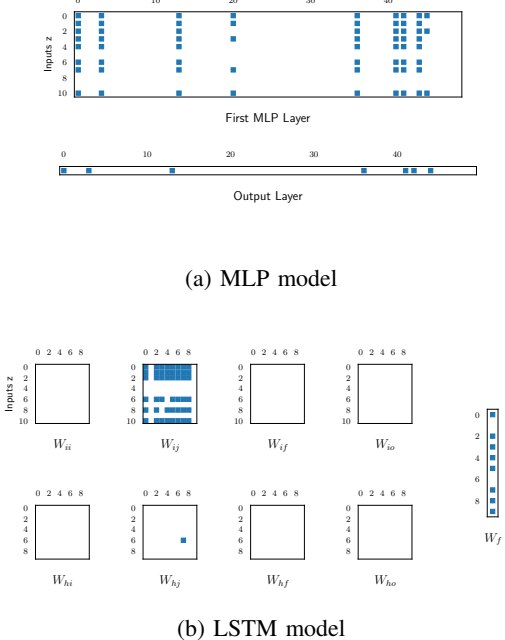
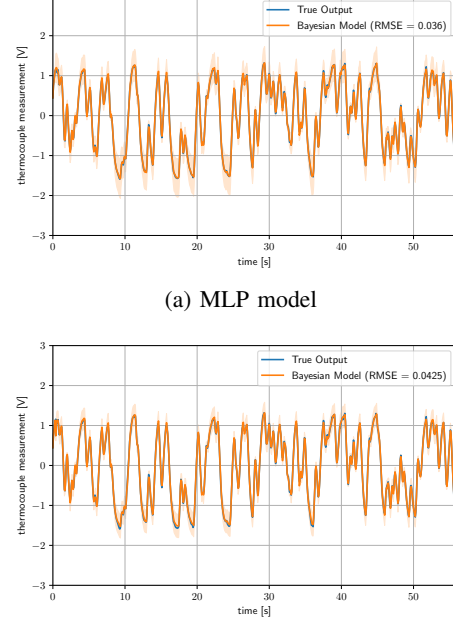


Fig. 9: The comparison on simulation result for different datasets

input and output lags chosen for the regressors are both 5. Models are inferred through $K_{\max} = 6$ identification cycles. The best validated model is obtained in the 5th cycle of identification with a sparsity of 88.1%. The model sparsity plot is shown in Fig. 10a. Furthermore, an RNN network is randomly initialized with one layer and 10 hidden LSTM units and no bias term. l_u and l_y are set to 5. The 6th and final identification cycle lead to the sparsest and best validated model with a sparsity of 93.5 %. Fig. 10b shows the final model sparsity plot.

Plots of the posterior predictive distribution's mean prediction and standard deviation obtained by sampling 10000 times from the posterior distribution of the connections' weights and by using Eq. (32) and (36) are shown in Fig. 11a and 11b. Plots of the identified models' free run simulations can be found in Fig. 9a.

Fig. 10: Model sparsity plot of the identified MLP and LSTM on Hairdryer dataset. *Blue* indicates non-pruned connections and *white* indicate pruned ones.Fig. 11: The identified MLP and LSTM model's output posterior mean predictions ($\pm 2\sigma$) on Hairdryer dataset.

APPENDIX F HEAT EXCHANGER

A heat exchanger is a thermodynamic device that ensures a transfer of heat in between two fluids seperated

by a wall. In this experiment, the dynamic relationship between the change in coolant temperature and the change in the product temperature is identified [11]. The first 3000 data points are used for identification and the remaining 2000 for validation. This dataset is particularly unique among the others. The process exhibits a delay of around 1/4 of a minute [11].

One hidden-layer MLP with 50 nodes is initialised with a linear activation function and no bias term. The lag chosen is $l_u = l_y = 150$ samples corresponding to the delay of 0.25 seconds that can be observed in the first instance of the given dataset. The experiment is run for 6 identification cycles, in which the 4th model is selected as the best validated model. The model is 99.3% sparse.

One layer RNN network with 10 LSTM units is trained with the same lag used previously ($l_u = l_y = 150$). The best validated model is the second out of 6 identification cycles. The accepted model's sparsity is 96.4 % for which the sparsity plot is given in Fig. 12b.

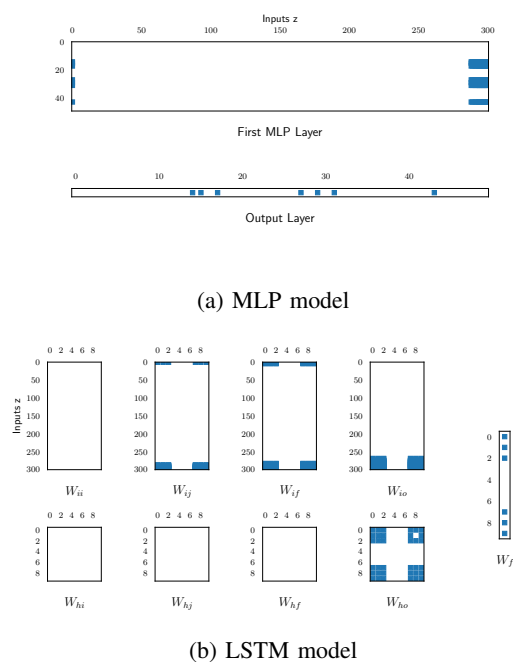
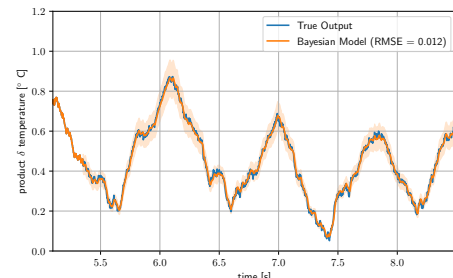


Fig. 12: Model sparsity plot of the identified MLP and LSTM on Heat Exchanger dataset.

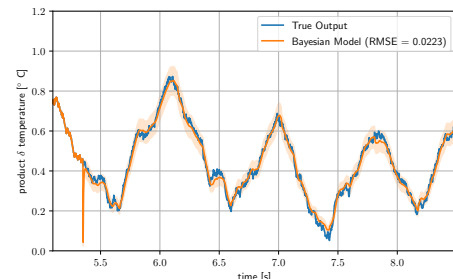
The predictive mean and standard deviation of the posterior predictive distribution are shown in Fig. 13a-13b against the real validation signal. These are obtained using 10000 samples of the posterior distribution. Please refer to Fig. 9b, for a plot of these free run simulations.

APPENDIX G GLASS TUBE MANUFACTURING PROCESS

In the process of manufacturing glass tubes, the melted glass shapes around a rotating cylinder, while homogenizing. Then it is drawn on rollers to a certain length. The thickness of the obtained glass tube is measured by a laser beam outside the chamber [39]. The objective is to identify the linear dynamic relationship between the input drawing speed and the output thickness. The datasets are



(a) MLP model



(b) LSTM model

Fig. 13: The identified MLP and LSTM model's output posterior mean predictions ($\pm 2\sigma$) on Heat Exchanger dataset.

provided by the MATLAB example. These are detrended and decimated by four, to get rid of the high frequency components of the signal [12]. This results in a sampling time of 4 seconds. The data used for identification consist of the first 500 datapoints and remaining 175 datapoints are used for validation.

An MLP is randomly initialized with one hidden layer and 50 neurons. The input regressors are chosen such as $l_u = l_y = 5$. The activation function used is linear without a bias term. The final obtained model is 97.8 % sparse with a sparsity plot shown in Fig. 14a. This model is the third generated model out of 6 identification cycles.

With the same choice of regressors, an LSTM network is initialized with one layer of 10 LSTM units. The bias term is not used in this case. In the 6 identification cycles, the 6th generated model is the sparsest and have the best validation performance. The sparsity plot of this network is given by Fig. 14b. The model is 99% sparse, and the only non-pruned parameters in the model correspond to the input to cell state operator W_{ij} .

The one-step ahead prediction estimates and uncertainties are obtained by Monte Carlo sampling 10000 times from the posterior and are shown in Fig. 15a-15b as a representation of the posterior predictive distribution. The free run simulations of the generated models in this paper are presented in Fig. 9c.

APPENDIX H CASCADED TANKS

A pump drives water up from the reservoir to the upper tank of two vertically cascaded tanks. The upper and lower tanks are separated by a small opening allowing water to fill the lower tank. The lower tank and the

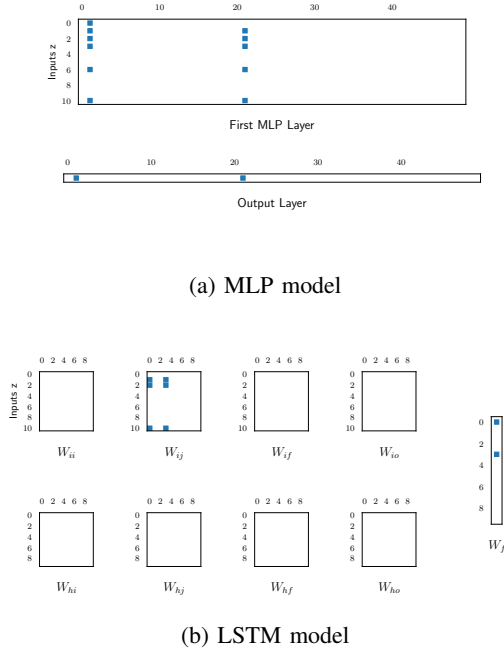


Fig. 14: Model sparsity plot of the identified MLP and LSTM on Glass Tube Manufacturing dataset.

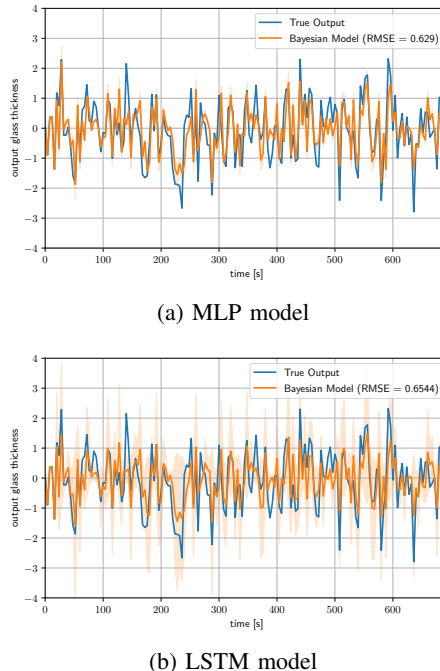


Fig. 15: The identified MLP and LSTM model's output posterior mean predictions ($\pm 2\sigma$) on Glass Tube Manufacturing dataset.

reservoir are also separated by a small opening, from which water goes back to the reservoir. In addition to that, water can overflow from the upper tank to the lower tank and reservoir. Water can also overflow the second tank and drop into the reservoir. The small openings and overflows are sources of nonlinearity [26]. The objective of the benchmark is the identification of the dynamic relationship between the input voltage to the pump and

the output measured water level in the lower tank by a capacitive sensor [26]. Two multisine input datasets and their corresponding outputs with a sampling rate of 4 seconds are provided. The datasets contain 1024 samples and are with different initial conditions. One of the datasets is used for estimation and the other for validation. The signals provided exhibit a static bias that is dealt with in the preprocessing stage of the identification procedure by detrending.

A three hidden layers deep MLP network with 10 neurons per layer is randomly initialized. The activation function used is the Rectified Linear Unit (ReLU) activation. The input regressors are selected as $l_u = l_y = 20$. The identification experiment is run for 10 cycles. The 9th generated model performs the best in validation with a sparsity of 84.5%. The model's sparsity plot is shown in Fig. 16a.

Moreover, a one-layer RNN with 10 LSTM units is also used as a model structure for the identification experiment. The 4th identified model with 60.3% sparsity turns out to be the best validated model out of 10 identification cycles. The sparsity plot of the corresponding model is shown in Fig. 16b.

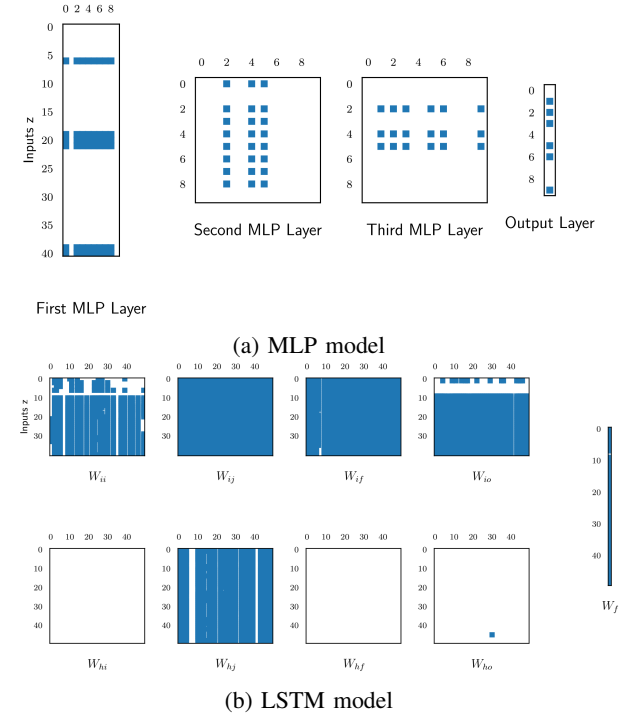
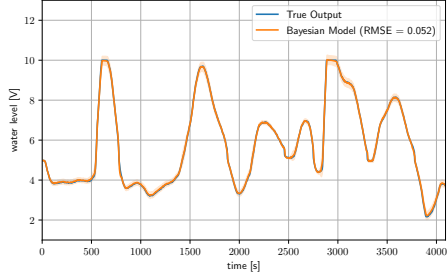


Fig. 16: Model sparsity plot of the identified MLP and LSTM on Cascaded Tanks dataset.

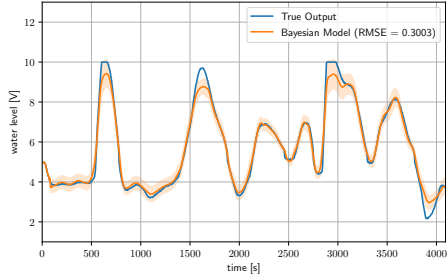
In addition, the posterior predictive mean and standard deviation are given in Fig. 17a and 17b. These are obtained by averaging Eqs 32 and 36 and sampling 50000 times from the inferred posterior distribution of the weights. A plot of the models' free run simulations is given in Fig. 9d.

APPENDIX I COUPLED ELECTRIC DRIVES

The coupled electric drives consist of two electric motors and a pulley, connected by a flexible belt forming



(a) MLP model



(b) LSTM model

Fig. 17: The identified MLP and LSTM model's output posterior mean predictions ($\pm 2\sigma$) on Cascaded Tanks dataset.

a triangle. The pulley is attached by a spring to a fixed frame. This results in belt tension, slippage, and pulley speed that is harder to model. In addition to that, the output pulley rotational speed is measured in ticks per second, insensitive to rotational directions. The dynamic relationship to be identified is between the input motors voltage and the measured rotational speed of the pulley. For this identification task, two uniformly distributed signals of 500 samples is provided spanning 10 seconds. With each of these datasets, the first 300 samples are used for estimation and the remaining for validation.

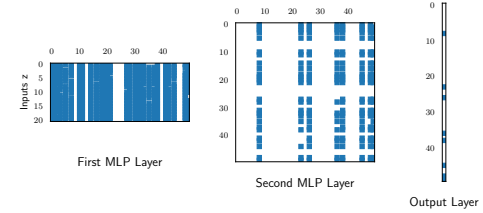
Two hidden layers MLP with 50 neurons each and ReLu activation functions is randomly initialized and trained with the estimation data for 10 identification cycles. The model's regressors are chosen such that $l_u = l_y = 10$. The model obtained in the 6th identification iteration is the chosen best model. This model is 78.4% sparse for which the sparsity plot is shown in Fig. 18a.

The same regressors are used for the identification of RNN model structure. An RNN with one layer and 10 LSTM units is trained for 10 identification cycles. The 8th identification yields the best simulation validation results. The resulting model is 72.8% sparse with the sparsity plot depicted in Fig. 18b.

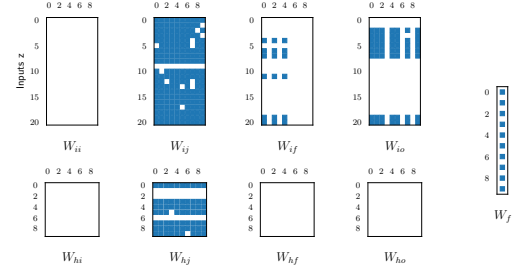
By using Eqs. (32) and (36), the mean and standard deviation of the posterior predictive distributions are plotted in Fig. 19a, 19c, 19b and (19d) for both validation datasets. These are obtained with Eqs. (32) and (36) and 50000 samples of the posterior distribution. The figures showing the resulting free run simulations are Fig. 9e-9f.

REFERENCES

[1] H.Ritter A.Botev and D.Barber. Practical gauss-newton optimisation for deep learning. In *Proceedings of the 34th International*



(a) MLP model



(b) LSTM model

Fig. 18: Model sparsity plot of the identified MLP and LSTM on Coupled Electric Drives dataset.

Conference on Machine Learning - Volume 70, ICML'17, pages 557–565. JMLR.org, 2017.

[2] A.Chiuso and G.Pillonetto. A Bayesian approach to sparse dynamic network identification. *Automatica*, 48(8):1553–1565, 2012.

[3] A.Delgado, C.Kambhampati, and K.Warwick. Dynamic recurrent neural network for system identification and control. *IEE Proceedings-Control Theory and Applications*, 142(4):307–314, 1995.

[4] A.G.Wilson. The case for Bayesian deep learning. *arXiv preprint arXiv:2001.10995*, 2020.

[5] A.Svensson and T.B.Schön. A flexible state-space model for learning nonlinear dynamical systems. *Automatica*, 80:189–199, 2017.

[6] G.Beintema, R.Toth, and M.Schoukens. Nonlinear state-space identification using deep encoder networks. In *Learning for Dynamics and Control*, pages 241–250. PMLR, 2021.

[7] G.Castellano and A.M.Fanelli. Variable selection using neural-network models. *Neurocomputing*, 31(1-4):1–13, 2000.

[8] H.V.H.Ayala, L.F. da Cruz, and R.Z.Freire et al. Cascaded free search differential evolution applied to nonlinear system identification based on correlation functions and neural networks. In *Proceedings of the 2014 IEEE Symposium on Computational Intelligence in Control and Automation (CICA)*, pages 1–7, Dec 2014.

[9] H.Zhou, M.Yang, and J.Wang et al. Bayesnas: A Bayesian approach for neural architecture search. In *Proceedings of the 36th International Conference on Machine Learning*, pages 7603–7613. PMLR, 2019.

[10] The MathWorks Incorporation. Estimating simple models from real laboratory process data. <https://nl.mathworks.com/help/ident/examples.html>. Accessed: 2020-11-25.

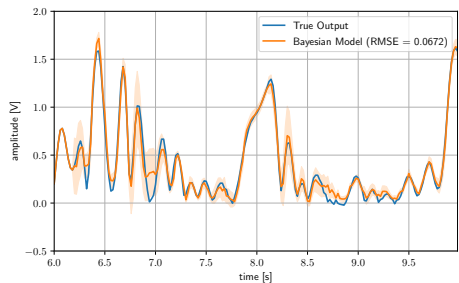
[11] The MathWorks Incorporation. Estimating transfer function models for a heat exchanger. <https://nl.mathworks.com/help/ident/examples.html>. Accessed: 2020-11-25.

[12] The MathWorks Incorporation. Glass tube manufacturing process. <https://nl.mathworks.com/help/ident/examples.html>. Accessed: 2020-11-25.

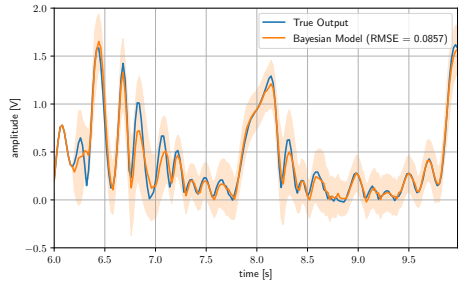
[13] J.Belz, T.Münker, and T.O.Heinz et al. Automatic modeling with local model networks for benchmark processes. *IFAC-PapersOnLine*, 50(1):470–475, 2017.

[14] J.Snoek, O.Rippel, and K.Swersky et al. Scalable Bayesian optimization using deep neural networks. In *Proceedings of the 2015 International Conference on Machine Learning*, pages 2171–2180. PMLR, 2015.

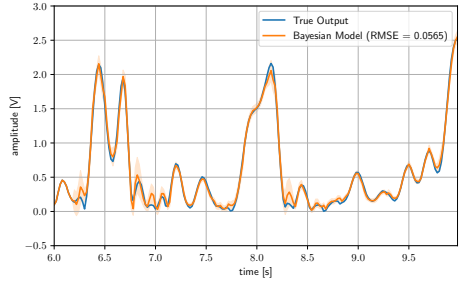
[15] J.Willard, X.Jia, and S.Xu et al. Integrating physics-based modeling



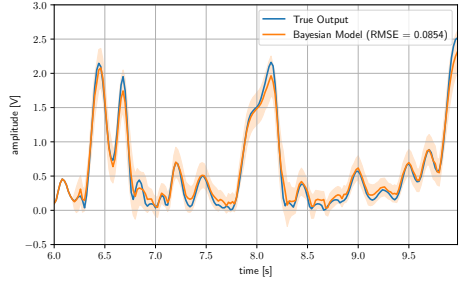
(a) MLP model on first validation dataset



(b) LSTM model on first validation dataset



(c) MLP model on second validation dataset



(d) LSTM model on second validation dataset

Fig. 19: The identified MLP and LSTM model's output posterior mean predictions ($\pm 2\sigma$) of Coupled Electric Drives on first and second validation dataset.

with machine learning: A survey. *arXiv preprint arXiv:2003.04919*, 2020.

[16] M.Stinchcombe K.Hornik and H.White. Multilayer feedforward networks are universal approximators. *Neural networks*, 2(5):359–366, 1989.

[17] L.Ljung. System identification. *Wiley encyclopedia of electrical and electronics engineering*, pages 1–19, 1999.

[18] L.Ljung. *System Identification: (2nd Ed.): Theory for the User 2nd Ed.* Prentice Hall PTR, USA, 1999.

[19] L.Ljung, C.Andersson, and K.Tiels et al. Deep learning and system identification. *IFAC-PapersOnLine*, 53(2):1175–1181, 2020.

[20] David J. C. MacKay. Bayesian interpolation. *Neural Computation*, 4(3):415–447, 1992.

[21] A.Janot M.Brunot and F.Carrillo. Continuous-time nonlinear systems identification with output error method based on derivative-

free optimisation. *IFAC-PapersOnLine*, 50(1):464–469, 2017.

[22] M.Leshno, V.Y.Lin, and A.Pinkus et al. Multilayer feedforward networks with a nonpolynomial activation function can approximate any function. *Neural Networks*, 6(6):861–867, 1993.

[23] M.Lindfors and T.Chen. Regularized lti system identification in the presence of outliers: A variational em approach. *Automatica*, 121:109152, 2020.

[24] M.Scarpiniti, D.Comminiello, and R.Parisi et al. Novel cascade spline architectures for the identification of nonlinear systems. *IEEE Transactions on Circuits and Systems I: Regular Papers*, 62(7):1825–1835, July 2015.

[25] M.Schoukens and F.G.Scheiwe. Modeling nonlinear systems using a volterra feedback model. In *Proceedings of the 2016 Workshop on Nonlinear System Identification Benchmarks*, 2016.

[26] M.Schoukens, P.Mattson, and T.Wigren et al. Cascaded tanks benchmark combining soft and hard nonlinearities. In *Workshop on nonlinear system identification benchmarks*, pages 20–23, 2016.

[27] R.Ge M.Zhou and C.Jin. A local convergence theory for mildly over-parameterized two-layer neural network. *arXiv preprint arXiv:2102.02410*, 2021.

[28] N.Simon, J.Friedman, and T.Hastie et al. A sparse-group lasso. *Journal of Computational and Graphical Statistics*, 22(2):231–245, 2013.

[29] D.Zachariah P.Mattsson and P.Stoica. Identification of cascade water tanks using a pwarx model. *Mechanical systems and signal processing*, 106:40–48, 2018.

[30] R.Karagoz and K.Batselier. Nonlinear system identification with regularized tensor network b-splines. *Automatica*, 122:109300, 2020.

[31] R.Rishi, K.Tiels, and A.Marconato et al. An unstructured flexible nonlinear model for the cascaded water-tanks benchmark. *IFAC-PapersOnLine*, 50(1):452–457, 2017. 20th IFAC World Congress.

[32] F.Sabahi and M. R. Akbarzadeh-T. Extended fuzzy logic: Sets and systems. *IEEE Transactions on Fuzzy Systems*, 24(3):530–543, June 2016.

[33] S.C.Nechita, R.Toth, and D.Khandelwal et al. Toolbox for discovering dynamic system relations via tag guided genetic programming, 2020.

[34] C.L.Giles S.Lawrence and A.C.Tsoi. What size neural network gives optimal generalization? convergence properties of backpropagation. Technical report, 1998.

[35] J.L.Proctor S.L.Brunton and J.N.Kutz. Discovering governing equations from data by sparse identification of nonlinear dynamical systems. *Proceedings of the National Academy of Sciences*, 113(15):3932–3937, 2016.

[36] T.Chen, M.S.Andersen, and L.Ljung et al. System identification via sparse multiple kernel-based regularization using sequential convex optimization techniques. *IEEE Transactions on Automatic Control*, 59(11):2933–2945, 2014.

[37] T.Gao, X.Gong, and K.Zhang et al. A recalling-enhanced recurrent neural network: Conjugate gradient learning algorithm and its convergence analysis. *Information Sciences*, 519:273–288, 2020.

[38] T.Wigren and M.Schoukens. *Coupled electric drives data set and reference models*. Department of Information Technology, Uppsala Universitet, 2017.

[39] G.Bastin V.Wertz and M.Haest. Identification of a glass tube drawing bench. *IFAC Proceedings Volumes*, 20(5):333–338, 1987.

[40] W.Pan, Y.Yuan, and J.S.Gonçalves et al. A sparse Bayesian approach to the identification of nonlinear state-space systems. *IEEE Transactions on Automatic Control*, 61(1):182–187, 2016.

[41] F.Menolascina W.Pan and G.B.Stan. Online model selection for synthetic gene networks. In *Proceedings of the 55th IEEE Conference on Decision and Control (CDC)*, pages 776–782. IEEE, 2016.

[42] W.R.Jacobs, T.Baldacchino, and T.Dodd et al. Sparse Bayesian nonlinear system identification using variational inference. *IEEE Transactions on Automatic Control*, 63(12):4172–4187, 2018.

[43] X.Ma, A.R.Triki, and M.Berman et al. A Bayesian optimization framework for neural network compression. In *Proceedings of the IEEE/CVF International Conference on Computer Vision*, pages 10274–10283, 2019.

[44] Y.Gal. *Uncertainty in Deep Learning*. PhD thesis, University of Cambridge, 2016.

[45] Y.Huang, C.Shao, and B.Wu et al. State-of-the-art review on Bayesian inference in structural system identification and damage assessment. *Advances in Structural Engineering*, 22(6):1329–1351, 2019.

[46] Y.Yuan, X.Tang, and W.Zhou et al. Data driven discovery of cyber physical systems. *Nature Communications*, 10(1):1–9, 2019.